Inverse synthetic aperture LADAR for geosynchronous space objects – signal-to-noise analysis

Casey J. Pellizzari
Air Force Research Laboratory (RDSMA) 535 Lipoa Parkway, Ste. 200, Kihei HI 96753
Charles L. Matson
Air Force Research Laboratory, Starfire Optical Range, Kirtland Air Force Base, NM 87117
Rao Gudimetla
Air Force Research Laboratory (RDSMA) 535 Lipoa Parkway, Ste. 200, Kihei HI 96753

ABSTRACT

Inverse synthetic aperture LADAR (ISAL) provides high resolution images which are not limited in resolution by the diffraction limit of the telescope collecting the imaging data. This makes it an ideal method for imaging Geosynchronous Earth Orbit (GEO) space objects. Although LADAR is a well researched topic, little has been published on the suitability of ISAL for imaging GEO space objects and the associated SNR models. This paper derives an expression for the return signal detected by a coherent ISAL system. Using tomographic techniques common to synthetic aperture radar (SAR), a model is developed for the signal-to-noise ratio of the reconstructed image. Noise sources considered include photon noise and laser speckle noise.

1. INTRODUCTION

Spotlight-mode Synthetic Aperture Radar (SAR) allows high resolution terrain imaging with microwaves using reasonably sized apertures. Similar concepts may be applied to laser radar (LADAR) for imaging Geosynchronous Earth Orbit (GEO) space objects using meter class apertures. Due to the distance of GEO objects (around 40Mm), conventional imaging systems require large apertures to resolve objects. Apertures on the order of 10m or more are required to provide useful information. Synthetic aperture systems utilize relative movement between the object and observer to synthesize larger apertures. For this reason, much smaller optics can be used, thereby reducing costs. Inverse synthetic aperture LADAR (ISAL) for imaging GEO space objects relies on small, relative movements of the object to form high resolution images using small telescopes. Just as large telescopes have their draw backs, so does ISAL. The difficulty and costs of obtaining a 10m class telescope have been traded for the difficulty and cost of actively illuminating a GEO object and coherently detecting the return signal. Therefore, it is important to fully understand the expected signal and noise levels for such a system. This paper derives the signal-to-noise ratio (SNR) for ISAL using first principles and an image processing viewpoint. The robust model can be used to predict future system performance and as an input for modeling ISAL post processing techniques.

2. BACKGROUND

Many imaging techniques using SAR and LADAR have been proposed. ISAL has three key characteristics which differentiate it from other techniques, making it suitable for imaging GEO objects. First, tomographic imaging techniques are used. Tomography has typically been associated with computer-aided-tomography (CAT) imaging found in medical applications [1]. Transmission tomography measures the energy that passes through an object to obtain a 2-D absorption profile of a 3-D object. Fig. 1(a) shows how the measured absorption creates a 1-D projection of the 2-D object. This projection is related to the object's Fourier transform by the Fourier Slice Theorem [1]. It states that the Fourier transform of a 1-D projection taken at angle θ is equal to a line (or slice) through the Fourier domain of the 2-D object. The line passes through the origin at an angle θ. Therefore, obtaining object projections for an infinite number of angles will allow perfect reconstruction of the 2-D Fourier transform, and therefore the 2-D object absorption profile from 1-D data. Fortunately, a finite number of projections can be used for practical use. Tomography allows 3-D images to be formed of an object's interior non-intrusively, making it very useful in medical imaging. Reflection tomography obtains 2-D projections of a 3-D object by measuring the reflected energy. Fig. 1(b) shows how the energy reflected from each point on the object creates a projection similar to transmission tomography. The differences are that the projection obtained by reflection is from the cross-range

direction (perpendicular to line-of-sight vector), and the profile obtained is only for the surface of the object. However, the data can still be processed the same way to reconstruct a 3-D object profile from 2-D reflection profiles.

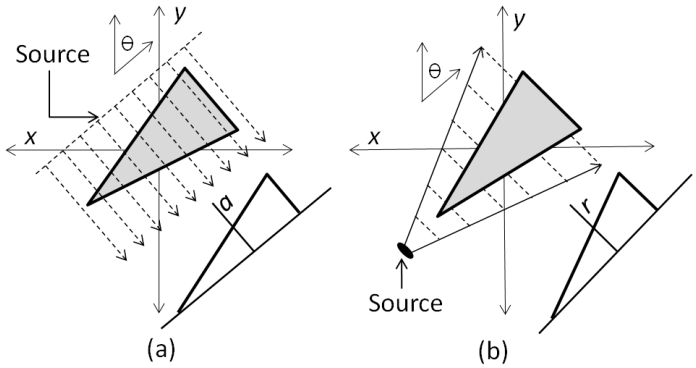

Fig. 1. Transmission tomography (a) measures the absorption profile of an object to recover a 1-D projection. Reflection tomography measures the reflected signal as a function of range to obtain a 1-D projection.

References [2, 3] show that tomography can be applied to SAR. This allows methods and algorithms developed for CAT to be used in SAR. In addition, the tomographic formulation simplifies SAR for the non-radar community and allows speckle phenomenon to be easily explained [22]. Tomography has also been applied to LADAR [4].

The second important characteristic that differentiates ISAL from other LADAR imaging techniques is coherent illumination and heterodyne detection, instead of direct detection [5]. This allows the object to be reconstructed from Fourier data which is offset from the origin, and obtained with a relatively small range of look angles. Image reconstruction from offset Fourier data is only possible for complex valued signals (coherent) [2]. Consider the complex object reflectivity and corresponding Fourier transform given by

$$r(x,y) = a(x,y)\exp[j\phi(x,y)], \tag{1}$$

$$R(u,v) = A(u,v) \otimes \mathrm{F}\{\exp[j\phi(x,y)]\}, \tag{2}$$

where $a(x,y)$ is the amplitude, $\phi(x,y)$ is the phase, and $\otimes$ indicates a convolution. If the phase is highly random due to surface fluctuations on the order of a wavelength, as seen in laser speckle, the Fourier transform of the exponential will be very broad. The convolution then spreads the amplitude information across a wide spectrum. Therefore, offset Fourier data will contain baseband (origin centered) information and a speckle image can be reconstructed from this information [2].

The final characteristic is that the ISAL waveform is chirped or linearly frequency-modulated (FM). Consider the outgoing signal

$$S(t,x,y) = Re\,\{E_s(x,y) * exp\,[i(2\pi f_0 t + \beta t^2)]\}, \tag{3}$$

where $E_s(x,y)$ is the amplitude, f_0 is the center frequency, and β/π is the chirp rate in Hz/s. The frequency, or first derivative of the phase, changes linearly with time. There are two advantages to using a chirped waveform. First, it has a large time-bandwidth product. The bandwidth is given by

$$B_c = \beta\tau_c/\pi, \tag{4}$$

where τ_c is the chirp duration [3]. From Eq. (4), it is clear that long pulses result in high bandwidths. This is an opposite result when compared to a continuous wave (CW) short burst, where a short pulse duration leads to high bandwidth. The large time-bandwidth product means that more energy can be transmitted, resulting in higher SNRs. The other advantage of a chirped waveform is that the processed return signal will be the Fourier transform of the object's reflectivity projection, offset from the origin as shown in Fig. 2. Image reconstruction will be possible from this offset data due to the random phase. The benefit of collecting offset Fourier data is apparent from the figure. A

more complete UV fill is obtained from the offset data, when compared to the baseband data. Baseband SAR and SAL systems require a wide range of look angles to reconstruct a useful image. For Low Earth Orbit (LEO) space objects, $\Delta\theta$ will be large, and baseband systems can be used [4]. However, the relative changes in angle for GEO objects are small. For this reason, ISAL is well suited for GEO imaging.

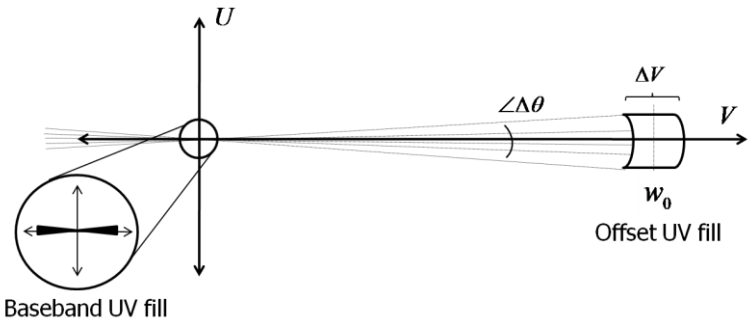

Fig. 2. Spatial frequency UV fill for look-angles in the range $\Delta\theta$. Only a small cone around the origin gets filled in for the baseband data. The offset data obtained by ISAL is more complete.

3. ANALYSIS

The following analysis is based on spotlight-mode SAR tomographic concepts presented in [3]. A similar analysis has been applied to SAL for planet imaging from satellite systems [8]. Although Lucke and Rickard help bridge the gap between the radar and optical imaging communities, their analysis is simplified and therefore their models lack generality and robustness [8]. This analysis seeks to develop a SNR model of ISAL in a general manner, using first principles where possible.

3.1 Basic Formulation

Consider the 2-D transmitter/receiver geometry shown in Fig. 3 with a transmitted signal given by Eq. (3). The instantaneous signal at the receiving aperture reflected from points between $-z_1$ and z_1 on the object, is given by

$$S_{reflected}(t,y) = Re\left\{\int_{-z_1}^{z_1} \alpha * o(y,z) * E_s[t-\tau(z),y] * \exp\left\{i2\pi\left[f_0\big(t-\tau(z)\big)+\beta\big(t-\tau(z)\big)^2\right]\right\} dz\right\}, \quad (5)$$

where α is a scaling coefficient accounting for signal loss due to atmospheric absorption, beam divergence to and from the object, and any transmission loss due to optics. $o(y,z)$ is the object field-reflectivity density (reflectivity over a small incremental range δz, centered at z), $\tau(z) =$ is the propagation time from point z to $z = 0$. The round trip propagation time to the center of the object and back, given by $\tau_0 = 2\,z_0/c$, has been left off for convenience. It is important to note that the chirp duration τ_c is much longer than the round trip propagation delay across the object and back given by $\tau_p = 2z_1/c$, where c is the speed of light. Equation (5) is only valid during the time [3]

$$-\frac{\tau_c}{2}+\frac{\tau_p}{2} \le t \le \frac{\tau_c}{2}-\frac{\tau_p}{2}. \quad (6)$$

During this period, the return signal contains information from the entire depth of the object and can be considered a convolution between the object's reflectivity profile and the transmitted pulse.

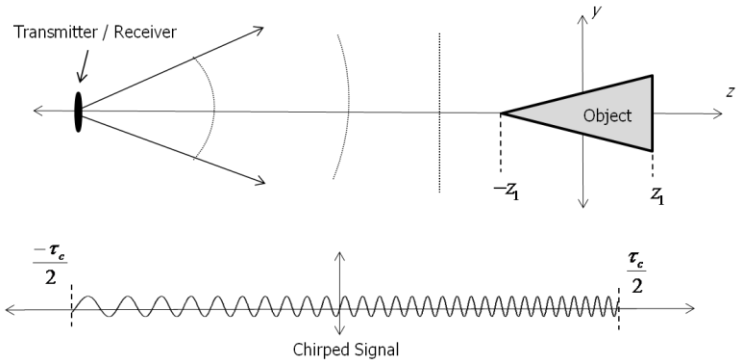

Fig. 3. Geometry used in ISAL analysis, along with chirped waveform over duration τ_c.

For heterodyne detection, the return signal is split and mixed with a local oscillator (LO) which consists of in-phase and quadrature versions of the FM chirp, given by

$$C_I(t) = \frac{1}{2}E_{LO}\cos[2\pi f_0(t-\tau_d) + \beta(t-\tau_d)^2], \tag{7}$$

$$C_Q(t) = -\frac{1}{2}E_{LO}\sin[2\pi f_0(t-\tau_d) + \beta(t-\tau_d)^2], \tag{8}$$

where τ_d is a deliberate, relative time delay between the LO and returning signal and E_{LO} is the amplitude of the LO. The time delay allows the temporal frequency content of the mixed (deramped) signal to be controlled. The ½ in Eqs. (7) and (8) result from one LO being split between the two detectors (in-phase and quadrature).

3.2 Analysis of In-Phase Intensity

The following section considers the in-phase channel. A similar analysis can be applied to the quadrature channel. After mixing, the intensity on the detector is given by

$$I_I(t,y) = \left|\frac{1}{2}S_{reflected}(t,y) + C_I(t)\right|^2, \tag{9}$$

$$\begin{aligned} I_I(t,y) = &\left\{\frac{1}{2}E_{LO} * cos[2\pi f_0(t-\tau_d) + \beta(t-\tau_d)^2]\right\}^2 \\ &+\left[\frac{1}{2}\int_{-z_1}^{z_1} \alpha * o(y,z) * E_s(t,y) * cos(2\pi\{f_0[t-\tau(z)] + \beta[t-\tau(z)]^2\})\,dz\right]^2 \\ &+2\int_{-z_1}^{z_1} \alpha * o(y,z) * \frac{1}{4}\sqrt{\eta_h}E_{LO} * E_s(t,y) * cos[2\pi f_0(t-\tau_d) + \beta(t-\tau_d)^2] * cos(2\pi\{f_0[t-\tau(z)] + \beta[t-\tau(z)]^2\})\,dz \end{aligned}, \tag{10}$$

where η_h is the heterodyne mixing efficiency [8]. The first term in Eq. (10) results in a direct current (DC) term and a cosine with frequencies centered at $2\omega_0$, which our detector will not respond to. Therefore, the first term will be

$$I_I(t,y)_{1st\ term} = \frac{E_{LO}^2}{8}. \tag{11}$$

The second can be written as

$$I_I(t,y)_{2nd\ term} = \frac{[\alpha * E_s(t,y)]^2}{8}\left\{\int_{-z_1}^{z_1} o(y,z)^2 dz + \iint_{-z_1}^{z_1} o(y,z)o(y,\hat{z}) * \cos\left[(z-\hat{z})\frac{2}{c}(\omega_0 - 2\beta t)\right] dz d\hat{z}\right\}, \tag{12}$$

where $\hat{z}$ is a dummy variable used for integration. At any time during the processing window, the second term gives a DC component for each point on the target weighted by the reflectivity squared. It also contains cross terms between all points on the object, with a frequency which depends on the separation of the two respective points. The beat frequencies which occur in this term range from zero where $z = \hat{z}$, to $\pm 8\beta z_1/c$, when the reflected signal

from the far ends of the object, $\pm z_1$ interfere. As will be seen later, this is the same frequency range as the third term which contains the desired signal. For GEO imaging, the return signal will be very weak compared to the LO ($\alpha * o(y,z) * E_s(t,y) \ll E_{LO}$) and the first and third terms of Eq. (10) will dominate. For this reason, the second term can be ignored. In addition, the time delay τ_d can be used to shift the frequencies of the desired signal so that the two terms don't overlap in bandwidth.

Finally, we consider the last term of Eq. (10). The two cosines can be expanded into two terms with frequencies given by

$$f_A = f_1 - f_2 = \frac{4\beta z}{c} - 2\beta\tau_d, \tag{13}$$

$$f_B = f_1 + f_2 = 2\omega_0 + 4\beta t - 2\beta\tau_d - \frac{4\beta z}{c}. \tag{14}$$

The lowest frequency will occur at the beginning of the processing window, given in Eq. (6). Substituting the lower value into Eq. (14) gives

$$f_B = 2\omega_0 - 2\beta\left[\tau_c - \left(\tau_p - \tau_d\right)\right] - \frac{4\beta z}{c}. \tag{15}$$

Assume that the chirp duration will be much longer than the round trip propagation time across the object and the deliberate time delay combined. That is, $\tau_c \gg \left(\tau_p - \tau_d\right)$. The second term in Eq. (14) becomes $2\pi B_c$. Since the bandwidth is much smaller than the center frequency, this term is negligible compared to the first. The last term will also be negligible compared to the first. This leaves

$$f_B \approx 2\omega_0. \tag{16}$$

Once again, our detector will not respond to such high frequencies. Therefore, only the cosine term with frequencies in the range of f_A will be detected. The third term of Eq. (10) reduces to

$$I_I(t,y)_{3rd\ term} = \frac{1}{4}\int_{-z_1}^{z_1} \alpha * o(y,z)\sqrt{\eta_h}E_{LO} * E_s\,(t,y) * \cos\left\{\left(z - \frac{c}{2}\tau_d\right)\frac{2}{c}[\omega_0 + 2\beta t] - \frac{4\beta z^2}{c^2} + \beta {\tau_d}^2\right\} dz, \tag{17}$$

The quadratic phase term $4\beta z^2/c^2$ acts to blur the image in the cross range dimension [3]. Through an example, Jakowatz states that as long as this term is below $\pi/4$, the blurring can be neglected. Even for relatively large GEO objects (50m) and high chirp rates (3GHz/s), this term will only be a few mrad and can be ignored. Finally, the last term in the phase can also be neglected if it is $\pi/4$ or less. This means the time delay is limited to

$$|\tau_d| < \sqrt{\pi/4\beta}\,. \tag{18}$$

Eq. (17) then becomes

$$I_I(t,y)_{3rd\ term} = \frac{\alpha\sqrt{\eta_h}E_{LO}E_s(t,y)}{4}\int_{-z_1}^{z_1} o(y,z) * \cos\left\{\left(z - \frac{c}{2}\tau_d\right)\frac{2}{c}[\omega_0 + 2\beta t]\right\} dz, \tag{19}$$

This term can be thought of as the real part of the Fourier transform of the object reflectivity with an additional phase term which is determined by τ_d. If we pull this additional phase term out of the integral over z, we can write

$$I_I(t,y)_{3rd\ term} = \frac{\alpha\sqrt{\eta_h}E_{LO}E_s(t,y)}{4} Re\left\{\exp[j\acute{z}Z]\int_{-z_1}^{z_1} o(y,z) * \exp(-jzZ)\,dz\right\}, \tag{20}$$

$$I_I(t,y)_{3rd\ term} = \frac{\alpha\sqrt{\eta_h}E_{LO}E_s(t,y)}{4} Re\{\exp[-j\acute{z}Z]\,O(y,Z)\}, \tag{21}$$

where $\acute{z} = \frac{c}{2}\tau_d$, and $Z = \frac{2}{c}(\omega_0 + 2\beta t)$. $O(y,Z)$ is the Fourier transform of the object's reflectivity-density function, for a given *y* [3]. The spatial frequency *Z* is a function of time. Therefore, at each time *t* during the processing window, the signal corresponds to the object's Fourier transform evaluated at a particular spatial frequency. Over the processing window, the range of *Z* is given by

$$\frac{2}{c}[\omega_0 - \beta\tau_c] \leq Z \leq \frac{2}{c}[\omega_0 + \beta\tau_c], \tag{22}$$

and therefore the spatial frequency bandwidth is

$$\Delta Z = \frac{4\pi B_c}{c}. \tag{23}$$

This offset Fourier data is centered at $2\omega_0/c$.

3.3 Detector Output

The current leaving the in-phase detector is given by [8]

$$i_I(t) = \eta_d \frac{q_e}{hv} \int \frac{1}{2} * I_I(t, y) dy, \tag{24}$$

where η_d is the detector quantum efficiency, q_e is the charge of an electron, h is Planck's constant, and v is the optical frequency. If the second term is ignored in Eq. (10), the current becomes

$$i_I(t) = \frac{\eta_d q_e}{2hv} \int \left[\frac{E_{LO}^2}{8} + \frac{1}{4} \int_{-z_1}^{z_1} \alpha * o(y, z) \sqrt{\eta_h} E_{LO} * E_s(t, y) * \cos\left\{ \left(z - \frac{c}{2}\tau_d \right) \frac{2}{c} [\omega_0 + 2\beta t] \right\} dz \right] dy, \tag{25}$$

For simplicity assume that the amplitude of the return signal is uniform across y, and thus the integrated current becomes

$$i_I(t) = \frac{\eta_d q_e}{2hv} A_{det} \left[\frac{E_{LO}^2}{8} + \frac{1}{4} \int_{-z_1}^{z_1} \alpha * o(z) \sqrt{\eta_h} E_{LO} * E_s(t) * \cos\left\{ \left(z - \frac{c}{2}\tau_d \right) \frac{2}{c} [\omega_0 + 2\beta t] \right\} dz \right], \tag{26}$$

where A_{det} is the area of the detector. The average electric field amplitudes are related to the average number of photons N by

$$\bar{E} = \sqrt{\frac{2hvN}{A_{det}\tau}}, \tag{27}$$

where the integration time is $\tau = (\tau_c - \tau_p)$ [8]. Using Eq. (27), the current becomes

$$i_I(t) = \frac{\eta_d q_e}{8\tau} \left[N_{LO} + 2\alpha * \sqrt{\eta_h N_{LO} N_s} * \int_{-z_1}^{z_1} o(z) * \cos\left\{ (z - z') \frac{2}{c} [\omega_0 + 2\beta t] \right\} dz \right]. \tag{28}$$

Finally, the current from the in-phase and quadrature detectors can be combined to represent a complex signal given by

$$i(t) = \frac{\eta_d q_e}{8\tau} \left[N_{LO}(1 + j) + 2\alpha * \sqrt{\eta_h N_{LO} N_s} * \int_{-z_1}^{z_1} o(z) * \exp\left\{ -j(z + z') \frac{2}{c} [\omega_0 + 2\beta t] \right\} dz \right], \tag{29}$$

3.4 Processing the Detector Output

After the bias is subtracted, the signal represents a scaled and phase shifted Fourier transform of the object's reflectivity density function. To recover the object's reflectivity profile, and therefore the image, the inverse Fourier transform is taken. Equation (29) can be written to group the time varying factors in the phase

$$\hat{\imath}(t) = k \int_{-z_1}^{z_1} o(z) * \exp\left(-j2\pi \left\{ \frac{4\breve{\beta}(z + \acute{z})}{c} t + \frac{2(z + \acute{z})}{c} f_0 \right\} \right) dz, \tag{30}$$

where $\hat{\imath}$ is the mean removed current, $\breve{\beta} = \beta/2\pi$, and

$$k = \frac{\alpha * \eta_d q_e}{4 * \tau} \sqrt{\eta_h * N_{LO} * N_s}. \tag{31}$$

A variable substitution can be made where

$$f = \frac{4\breve{\beta}(z+\acute{z})}{c}, \tag{32}$$

is the temporal beat frequency from point z on the object, and Eq. (30) becomes

$$\hat{\imath}(t) = k\int_{-f_1}^{f_1} \frac{o\left(\frac{fc}{4\breve{\beta}}+\acute{z}\right)}{\frac{c}{4\breve{\beta}}} * \exp\left[-j2\pi\left(ft + \frac{ff_0}{2\breve{\beta}}\right)\right]\frac{c}{4\breve{\beta}}df. \tag{33}$$

$o(z)$ is the reflectivity per δz increment, where $\delta z = z_1 - z_2$. When changing variables, this becomes the reflectivity per δf given by

$$\delta f = \frac{c}{4\breve{\beta}}(f_1 - f_2). \tag{34}$$

The $c/4\breve{\beta}$ factors in the integral cancel each other out. We now take the inverse Fourier transform the signal given by

$$I(f) = \int_{-\tau/2}^{\tau/2} k\int_{-\acute{f}_1}^{\acute{f}_1} o\left(\frac{\acute{f}c}{4\breve{\beta}} - \acute{z}\right)\exp\left[-j2\pi\left(ft + \frac{ff_0}{2\breve{\beta}}\right)\right]d\acute{f}\exp(2\pi jft)dt, \tag{35}$$

where $\acute{f}$ is a dummy variable used for integration. Now the order of integration is switched and the exponentials are combined to get

$$I(f) = k\int_{-\acute{f}_1}^{\acute{f}_1} o\left(\frac{\acute{f}c}{4\breve{\beta}} - \acute{z}\right)\int_{-\tau/2}^{\tau/2}\exp\left[-j2\pi\left(ft + \frac{ff_0}{2\breve{\beta}}\right)\right]dtd\acute{f}, \tag{36}$$

Next, the non-time-varying terms in the exponential is moved outside the integral.

$$I(f) = k\int_{-\acute{f}_1}^{\acute{f}_1} o\left(\frac{\acute{f}c}{4\breve{\beta}} - \acute{z}\right)\exp\left(j2\pi\frac{\acute{f}f_0}{2\breve{\beta}}\right)\int_{-\tau/2}^{\tau/2}\exp\left(-j2\pi(\acute{f}+f)t\right)dtd\acute{f}, \tag{37}$$

The integration can now be carried out.

$$I(f) = k\int_{-\acute{f}_1}^{\acute{f}_1} o\left(\frac{\acute{f}c}{4\breve{\beta}} - \acute{z}\right)\exp\left(j2\pi\frac{\acute{f}f_0}{2\breve{\beta}}\right)\int_{-\tau/2}^{\tau/2}\{\cos[2\pi(\acute{f}+f)t] + i\sin[2\pi(\acute{f}+f)t]\}dtd\acute{f}, \tag{38}$$

$$I(f) = k\int_{-\acute{f}_1}^{\acute{f}_1} o\left(\frac{\acute{f}c}{4\breve{\beta}} - \acute{z}\right)\exp\left(j2\pi\frac{\acute{f}f_0}{2\breve{\beta}}\right)\,2\frac{\sin[\tau\pi(\acute{f}+f)]}{\pi(\acute{f}-f)}d\acute{f}, \tag{39}$$

For convenience, we can multiply the last factor by τ/τ to create a sinc function

$$I(f) = \tau k\int_{-\acute{f}_1}^{\acute{f}_1} o\left(\frac{\acute{f}c}{4\breve{\beta}} - \acute{z}\right)\exp\left(j2\pi\frac{\acute{f}f_0}{2\breve{\beta}}\right)\,\mathrm{sinc}[\pi\tau(\acute{f}+f)]d\acute{f}, \tag{40}$$

Had the Fourier transform been taken for an infinite signal (i.e. $\tau = \infty$), the sinc function would become a delta function with zero width. This delta function would perfectly sample the object reflectivity for each frequency over the given integral. However, the sinc has a central lobe width of $2/\tau$ with "ringing" past that. This acts to blur and distort the sampled frequencies. Since these frequencies represent different ranges on the object, the reconstructed image is blurred in range. Using the derivative of Eq. (32) we can relate the blur in frequency to the blur in range by substituting $df_{sinc} = 2/\tau$.

$$dz_{sinc} = \frac{(2/\tau)c}{4(\beta/2\pi)} = \frac{c\pi}{\tau\beta}, \tag{41}$$

Figure 4 shows how the sinc function's central-lobe width changes with integration time for two different chirp rates. The blur in range decreases as the integration time increases. However, it is important to note that the resolution will also increase. Reference [3] gives the range resolution as

$$\delta z = \frac{c}{2B_c}. \tag{42}$$

If we divide the sinc's width by the range resolution, the result is

$$\frac{dz_{sinc}}{\delta z} = \frac{2\tau_c}{\tau}, \tag{43}$$

where Eq. (4) has been used. Finally, $\tau_c/(\tau_c - \tau_p) \approx \tau_c$, thus the blur caused by the finite integration time will always result in a blur of two pixels.

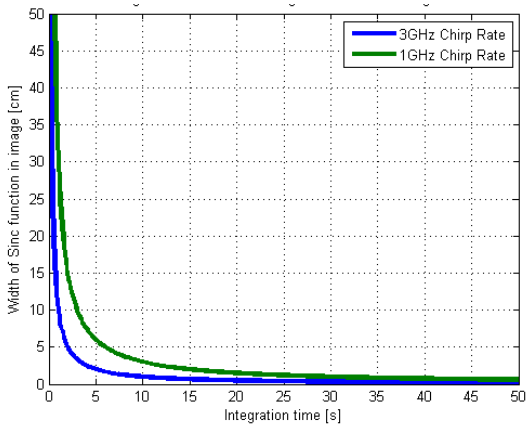

Fig. 4. Blur in range z as a function of integration time for two different chirp rates.

As the integration time increases, the sinc's width will be small compared to significant changes on the object's profile. Therefore, the sinc function can be modeled as a Dirac delta function and Eq. (40) becomes

$$I(f) = k\tau \int_{-\acute{f}_1}^{\acute{f}_1} o\left(\frac{\acute{f}c}{4\beta} + \acute{z}\right) \exp\left(j2\pi \frac{\acute{f}f_0}{2\beta}\right) \delta(\acute{f} + f) d\acute{f}. \tag{44}$$

Carrying out the integration leaves

$$I(f) = k\tau * o\left(\frac{fc}{4\beta} + \acute{z}\right) \exp\left(j2\pi \frac{ff_0}{2\beta}\right), \tag{45}$$

where the integration over $\acute{f}$ has changed $o(f)$ from a reflectivity density, to a unit-less reflectivity. Equation (32) is used to change variables back to z, giving

$$I(z) = \frac{\alpha * \eta_d q_e}{4} \sqrt{\eta_h * N_{LO} * N_s} o(z) \exp\left\{j\left[\frac{2(z+\acute{z})\omega_0}{\pi c}\right]\right\}. \tag{46}$$

The difference between $I(f)$ and $I(z)$ can be confusing. The two are the same function, just evaluated at different frequencies. $I(z)$ is simply $I\left(f = \frac{2\beta}{\pi c} z\right)$. The end result is a scaled and phase-shifted version of the object reflectivity along the z axis. The last factor applies a phase to each range element. This results from the time delay and shifting the signal to baseband prior to the inverse Fourier transform. Finally, we estimate 1-D object reflectivity. To do this, the extra factors are divided out and the magnitude squared is taken.

$$\hat{o}(z) = \left| \frac{I(z)}{\left(\frac{\alpha}{4}\right) * (\eta_d q_e \sqrt{\eta_h * N_{LO}})} \right|^2. \tag{47}$$

$$\hat{o}(z) = N_s o^2(z). \tag{48}$$

Here we see that the signal of interest is simply the energy spectral density (ESD) of the heterodyne output. This will be important when developing the stochastic model.

3.5 Reconstructed Image Using Backprojections

Although $\hat{o}(z)$ is a one-dimensional function of range, it actually represents a projection of the two dimensional object reflectivity function taken at angle θ [3]. A subscript $\hat{o}_\theta(z)$ is added to note the angle for which the return signal was measured. Figures 5 and 6 illustrate this concept. For angle θ, the LOS vector from the aperture to the object becomes z'. This is the direction of illumination and the slice of Fourier data contained in the return signal shown in Fig 5(c) is only a function of z'. Figure 6 provides the 1-D perspective of the object, return signal, and processed signal shown in Fig. 5. Figure 5 shows how this 1-D return signal is actually a line in the 2-D spatial frequency domain. In Fig. 5, the 2-D inverse Fourier transform, or backprojection [1] representing the processed signal for look angle θ, shows how the 1-D processed signal is "smeared" across the y-z plane at an angle θ. All points along lines parallel to y' have the same value for a single look angle.

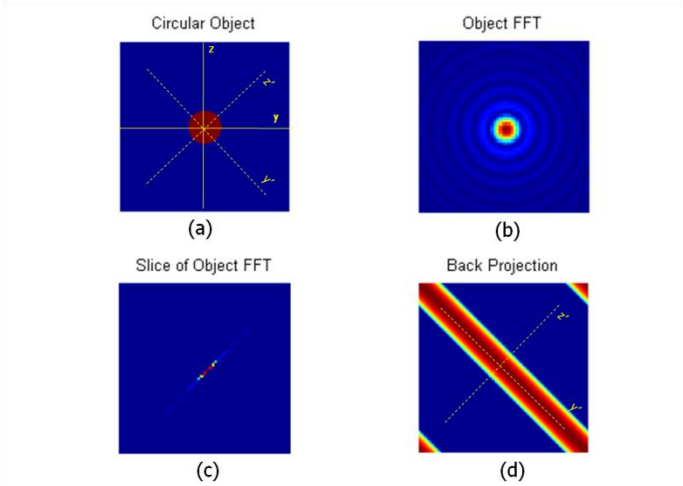

Fig. 5. (a) 2-D circular object in y-z plane with rotated axes z' and y' shown, (b) Fourier transform of (a), (c) single slice of (b) corresponding to the return signal along the z' axis, and (d) inverse Fourier transform of (c) with rotated axes shown.

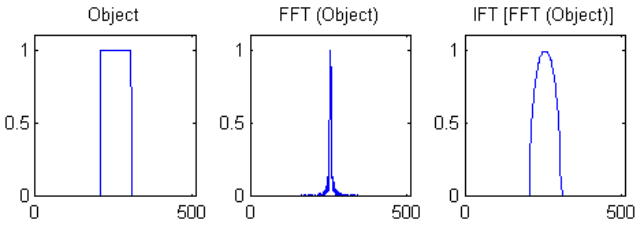

Fig. 6. (left) Simple 1-D example of rectangular object (slice of 2-D circle in Fig.5), (middle) Fourier transform of object, and (right) inverse Fourier transform of (middle)

For each look angle, a different backprojection is obtained. When combined, more information about the image is gained. Figure 7 demonstrates how the summation of backprojections (bottom row) improves the image. From these simple examples, it is clear that each pixel value in the z-y image plane is the sum of individual backprojections. We must mathematically determine the total contribution to each pixel in the y-z plane. First consider a single return and backprojection. For a given 1-D return we express the value of pixel (y,z) in the final image. The 1-D projection is smeared along the $\theta+\pi/2$ direction (orthogonal to z' axis) **[1]**. The value of the 1-D return at point z' is given to each pixel in the 2-D array which lies along the line $z = (\tan\theta)y + (\sec\theta)z'$. For a pixel at location (y_1, z_1) in the 2-D image $|g(y,z)|^2$, the value contributed from a single backprojection is given by

$$|g_\theta(y_1,z_1)|^2 = |\hat{o}_\theta(z' = z_1\cos\theta - y_1\sin\theta)|^2 = \left|\sqrt{N_s}o(z_1\cos\theta - y_1\sin\theta)\exp\left[\frac{j2(z_1\cos\theta - x_1\sin\theta)\omega_0}{\pi c}\right]\right|^2. \quad (49)$$

The value of each pixel in the final reconstructed image (composed of all measured look angles) is given by

$$|g(y,z)|^2 = \left|\sum_{n_\theta=1}^{N_\theta} \sqrt{N_s}\, o(z_1 \cos\theta - y \sin\theta) \exp\left[\frac{i2(z_1 \cos\theta - x_1 \sin\theta)\omega_0}{\pi c}\right]\right|^2, \tag{50}$$

where the angle $\theta = n_\theta * \delta\theta$, N_θ is the total number of look angles, and $\delta\theta = N_\theta / n_\theta$. For additional information about techniques such as convolution backprojection (CBP) which can improve the final image quality, the reader may consult [1, 3, 9].

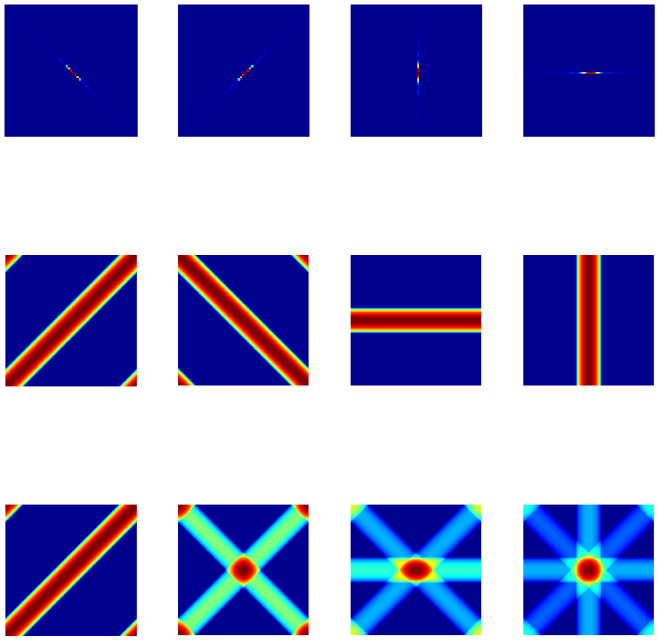

Fig. 7. From the object in Fig. 5, slices of the 2-D spatial-frequency domain for different look angles (top row) are inverse Fourier transformed (middle row), and added together to form an image (bottom row).

3.6 Signal-to-Noise Ratio

The dominate noise sources for heterodyne detection are laser speckle noise and shot noise. Both background and detector noise can be neglected [10]. As will be shown, the electro-magnetic (EM) field that is incident on the detector has circularly complex Gaussian statistics and the detector output has Poisson statistics which depend on the speckle field intensity [11, 12]. The detector output can therefore be modeled as a doubly stochastic Poisson process as described by [12]. A doubly stochastic Poisson process is a Poisson process with a random rate function. For ISAL, the Poisson rate function $\lambda(t)$ is the complex detector output given by Eq. (29), divided by q_e to get the number of photo-electron events.

$$\lambda(t) = \frac{i_I(t) + j i_Q(t)}{q_e} \tag{51}$$

If the z and z' terms in the cosine and sine of Eq. (51) are expanded, the z' terms can be moved out of the integral, and the rate function can be written as

$$\lambda(t) = \frac{\eta_d}{8\tau}\left\{N_{LO}(1+j) + 2\alpha\sqrt{\eta_h * N_{LO} * N_s}\exp\left[\frac{j2z'}{c}(\omega_0 + 2\beta t)\right]\int_{-z_1}^{z_1} o(z)\left\{\cos\left[\frac{-2z}{c}(\omega_0 + 2\beta t)\right] + j\sin\left[\frac{-2z}{c}(\omega_0 + 2\beta t)\right]\right\} dz\right\}, \tag{52}$$

If we consider integrating over a range dz large compared to a wavelength but small compared to changes in the signal envelope, we can model the return signal as a planar-surface laser speckle problem [13] which is thoroughly treated by [11, 12]. The random fluctuations in z of the rough object surface will create randomness in the return signal. In Eq. (52) both $o(z)\cos\left[\frac{2z}{c}(\omega_0 + 2\beta t)\right]$ and $o(z)\sin\left[\frac{2z}{c}(\omega_0 + 2\beta t)\right]$ represent random phasor sums integrated over y in Eq. (26), and can be considered zero-mean independent and identically distributed Gaussian random variables [12], assuming that $2\beta t \ll \omega_0$. The complex rate function is therefore a circular complex Gaussian random variable, with mean $N_{LO}(1+j)$.

The rate function and corresponding ESD, $\mathbb{E}_\Lambda(f)$ can be expressed as

$$\lambda(t) = \frac{\eta_d}{8\tau} N_{LO}(1+j) + \hat{\imath}(t)\ , \tag{53}$$

$$\mathbb{E}_\Lambda(f) = \mathrm{E}\{|\Lambda(f)|^2\} = \mathrm{E}\left\{\left|\frac{\eta_d}{8} N_{LO}(1+j)\delta(f) + I(f)\right|^2\right\}, \tag{54}$$

$$\mathbb{E}_\Lambda(f) = \mathrm{E}\{\Lambda(f)\Lambda^*(\zeta)\} = \mathrm{E}\left\{\left[\frac{\eta_d}{8} N_{LO}(1+j)\delta(f) + I(f)\right]\left[\frac{\eta_d}{8*\tau} N_{LO}(1-j)\delta(\zeta) + I^*(\zeta)\right]\right\}, \tag{55}$$

$$\mathbb{E}_\Lambda(f) = \mathrm{E}\left\{2\left(\frac{\eta_d}{8} N_{LO}\right)^2 \delta(f)\delta(\zeta) + \frac{\eta_d}{8*\tau} N_{LO}(1-j)\delta(\zeta)I(f) + \frac{\eta_d}{8*\tau} N_{LO}(1+j)\delta(f)I^*(\zeta) + I(f)I^*(\zeta)\right\}, \tag{56}$$

$$\mathbb{E}_\Lambda(f) = 2\left(\frac{\eta_d}{8} N_{LO}\right)^2 \delta(f)\delta(\zeta) + \frac{\eta_d}{8*\tau} N_{LO}(1-j)\left\{\delta(\zeta)\mathrm{E}[I(f)] + \delta(f)\mathrm{E}\{I^*(\zeta)\}\right\} + \mathrm{E}\{I(f)I^*(\zeta)\}, \tag{57}$$

where

$$\mathrm{E}\{I(f)\} = \mathrm{E}\left\{\frac{\alpha*\eta_d}{4}\sqrt{\eta_h * N_{LO} * N_s}\, o\left(\frac{fc}{4\vec{\beta}} - \acute{z}\right)\exp\left(i2\pi\frac{ff_0}{2\vec{\beta}}\right)\right\}, \tag{58}$$

Just as we did above to model the laser speckle in Eq. (52), we can expand Eq. (58) in a similar way using Eq. (32). Therefore, Eq. (58) becomes

$$\mathrm{E}\{I(f)\} = \frac{\alpha*\eta_d}{4}\sqrt{\eta_h * N_{LO} * N_s}\exp\left(\frac{i\acute{z}\omega_0}{\pi c}\right)\mathrm{E}\left\{o(z)\exp\left(\frac{iz\omega_0}{\pi c}\right)\right\}, \tag{59}$$

Just as before, the factors inside the expectation can be treated as a circular complex Gaussian random variable, and $\mathrm{E}\{I(f)\} = 0$. Next, let us find the second moment.

$$\mathrm{E}\{I(f)I^*(\zeta)\} = \mathrm{E}\left\{k^2 o\left(\frac{f\pi c}{2\beta} - \acute{z}\right)\exp\left(i\frac{f\omega_0}{2\beta}\right) o\left(\frac{\zeta\pi c}{2\beta} - \acute{z}\right)\exp\left(-i\frac{\zeta\omega_0}{2\beta}\right)\right\}, \tag{60}$$

where

$$k = \frac{\alpha*\eta_d}{4}\sqrt{\eta_h * N_{LO} * N_s}\exp\left(\frac{i2\acute{z}\omega_0}{\pi c}\right). \tag{61}$$

For $f \neq \zeta$ the second moment is

$$\mathrm{E}\{I(f)I^*(\zeta)\} = k^2\mathrm{E}\left\{o\left(\frac{f\pi c}{2\beta} + \acute{z}\right)\exp\left(-i\frac{f\omega_0}{2\beta}\right)\right\}\mathrm{E}\left\{o\left(\frac{\zeta\pi c}{2\beta} + \acute{z}\right)\exp\left(i\frac{\zeta\omega_0}{2\beta}\right)\right\} = 0. \tag{62}$$

When $f = \zeta$,

$$\mathrm{E}\{I(f)I^*(\zeta)\} = k^2 o^2\left(\frac{f\pi c}{2\beta} + \acute{z}\right)\delta(f-\zeta). \tag{63}$$

Finally Eq. (57) becomes

$$\mathbb{E}_\Lambda(f) = 2\left(\frac{\eta_d}{8} N_{LO}\right)^2 \delta(f) + k^2 o^2(z). \tag{64}$$

Now that the rate function has been analyzed, we can consider shot noise. The ESD of the doubly stochastic Poisson process will give the mean signal in the image for a single projection (prior to the bias terms being removed). In this case the output of each detector, in-phase and quadrature, represents a complex Poisson impulse response with the complex signal expressed as [12]

$$i(t) = \sum_{n=1}^{N}\delta(t-t_n) + j\sum_{k=1}^{K}\delta(t-t_k). \tag{65}$$

and Fourier transform

$$\mathcal{I}(f) = \sum_{n=1}^{N}\exp(j2\pi f t_n) + j\sum_{k=1}^{K}\exp(j2\pi f t_k). \tag{66}$$

Goodman [12] shows that the energy spectral density for a doubly Poisson process can be expressed as

$$\mathbb{E}_\mathcal{I}(f) = \bar{K}_I + \mathbb{E}_{\Lambda_\mathrm{I}}(f) + \bar{K}_Q + \mathbb{E}_{\Lambda_\mathrm{Q}}(f), \tag{67}$$

where $\bar{K}_I$ and $\bar{K}_Q$ are the average number of photo-electrons generated by the in-phase and quadrature stochastic rate functions, respectively. If we assume identical detectors, then Eq. (67) can be written as

$$\mathbb{E}_{\mathcal{J}}(f) = 2\bar{K} + \mathbb{E}_{\Lambda}(f). \tag{68}$$

$\bar{K}$ can be found by time averaging either the real or imaginary part of the mean rate function [12]

$$\bar{K} = \int_{-\tau/2}^{\tau/2} \mathrm{E}[\mathrm{Re}\{\lambda(t)\}]dt = \int_{-\tau/2}^{\tau/2} \mathrm{E}[\mathrm{Im}\{\lambda(t)\}]dt = \mathrm{Re}\{\bar{\lambda}\}\tau = \mathrm{Im}\{\bar{\lambda}\}\tau. \tag{69}$$

$$\bar{K} = \frac{\eta_d}{8} N_{LO}. \tag{70}$$

Finally, the ESD can be expressed as

$$\mathbb{E}_{\mathcal{J}}(f) = \frac{\eta_d}{4} N_{LO} + 2\left(\frac{\eta_d}{8} N_{LO}\right)^2 \delta(f) + k^2 o^2 \left(\frac{f\pi c}{2\beta} + \acute{z}\right), \tag{71}$$

This result shows that the mean pixel value for each frequency (and respective range), is equal to the scaled return signal weighted by the object reflectivity, plus a bias term, representing the LO, and a spike at the origin due to the bias of the rate function. In the end, we wish to estimate just the signal of interest. This is given by

$$\mathbb{O}(z) = \frac{\mathbb{E}_{\mathcal{J}}\left(f = \frac{2\beta(z+\acute{z})}{\pi c}\right) - \frac{\eta_d}{4} N_{LO} - 2\left(\frac{\eta_d}{8} N_{LO}\right)^2 \delta\left(\frac{2\beta(z-\acute{z})}{\pi c}\right)}{\left[\frac{\alpha * \eta_d}{4}\sqrt{\eta_h * N_{LO}}\right]^2} = N_s o^2(z), \tag{72}$$

Now that the first moment $\mathbb{E}_{\mathcal{J}}(f)$ has been found, the second moment of $|\mathcal{J}(f)|^2$ is needed to find the variance, and corresponding SNR. In this case, that means finding the fourth order moment of the Fourier transform of a doubly stochastic Poisson process expressed as

$$\mathrm{E}\{|\mathcal{J}(f)|^4\} = \mathrm{E}\left\{\sum_{n=1}^{N}\sum_{m=1}^{M}\sum_{p=1}^{P}\sum_{q=1}^{Q} \exp(j2\pi f t_n)\exp(j2\pi f t_m)\exp(j2\pi f p)\exp\left(j2\pi f t_q\right)\right\}. \tag{73}$$

Fortunately for us, Ref. [12] has an entire appendix (Appendix C) devoted to this lengthy calculation. The final result is given by

$$\mathrm{E}\{|\mathcal{J}(f)|^4\} = \bar{K} + 2\bar{K}^2 + 4(1+\bar{K})\mathbb{E}_{\Lambda}(f) + \mathbb{E}_{\Lambda}(2f) + 2{\mathbb{E}_{\Lambda}}^2(f), \tag{74}$$

which makes the variance

$$\sigma^2_{|\mathcal{J}(f)|^2} = \bar{K} + \bar{K}^2 + 2\bar{K}\mathbb{E}_{\Lambda}(f) + 4\mathbb{E}_{\Lambda}(f) + \mathbb{E}_{\Lambda}(2f) + {\mathbb{E}_{\Lambda}}^2(f). \tag{75}$$

From above, $\bar{K}$ for a single Poisson process will be $2\bar{K}$ for a complex Poisson process when the real and imaginary parts have equal means. Equation (75) becomes

$$\sigma^2_{|\mathcal{J}(f)|^2} = 2\bar{K} + 4\bar{K}^2 + 4\bar{K}\mathbb{E}_{\Lambda}(f) + 4\mathbb{E}_{\Lambda}(f) + \mathbb{E}_{\Lambda}(2f) + {\mathbb{E}_{\Lambda}}^2(f). \tag{76}$$

Here we see what Ref. [12] calls the "half-frequency phenomenon" in the fifth term. The noise at frequency *f* has contributions from the signal present at 2*f*. However, this term can be ignored if the beat frequency bandwidth is smaller than the center beat frequency. In this case, the bandwidth will not overlap with any noise at the half-frequencies. For this to be the case, the negative time delay-distance $\acute{z}$ must be much greater than the object width. That is,

$$\Delta f < \frac{2}{3} f_0, \tag{77}$$

$$\acute{z} > 3z_1. \tag{78}$$

Once again, this shows that the LO time delay will reduce noise. However, the value of the time delay is bounded by both Eq. (18) and (78). In addition, the noise terms with $\delta(f)$ can be ignored since the beat frequency f will not be zero. Moving on, we substitute $\overline{K}$ and $\mathbb{E}_\Lambda(f)$ into Eq. (76) giving

$$\sigma^2_{|\mathcal{J}(z)|^2} = 2\left(\frac{\eta_d}{8}N_{LO}\right) + 4\left(\frac{\eta_d}{8}N_{LO}\right)^2 + 4\left(\frac{\eta_d}{8}N_{LO}\right)k^2o^2(z) + 4k^2o^2(z) + k^4o^4(z), \tag{79}$$

Since we divided the signal estimate by a constant in Eq. (72), the variance must be divided by the square of the same constant, giving

$$\sigma^2_{|\mathcal{J}(z)|^2} = \frac{2\left(\frac{\eta_d}{8}N_{LO}\right)+4\left(\frac{\eta_d}{8}N_{LO}\right)^2+4\left(\frac{\eta_d}{8}N_{LO}\right)k^2o^2(z)+4k^2o^2(z)+k^4o^4(z)}{\left[\frac{\alpha*\eta_d}{8}\sqrt{\eta_h*N_{LO}}\right]^4}. \tag{80}$$

Finally, the SNR for a single projection can be expressed as

$$SNR_\theta = \frac{\mathbb{O}(z)}{\sqrt{\sigma^2_{|\mathcal{J}(z)|^2}}}. \tag{81}$$

$$SNR_\theta = \frac{N_s o^2(z)}{\sqrt{\frac{2\left(\frac{\eta_d}{8}N_{LO}\right)+4\left(\frac{\eta_d}{8}N_{LO}\right)^2+4\left(\frac{\eta_d}{8}N_{LO}\right)k^2o^2(z)+4k^2o^2(z)+k^4o^4(z)}{\left[\frac{\alpha*\eta_d}{4}\sqrt{\eta_h*N_{LO}}\right]^4}}}. \tag{82}$$

When the individual projections are "smeared" across the final image in the backprojection process, the statistics will not change. The above SNR is applicable to each pixel in the final image.

4. RESULTS

It is now useful to analyze Eq. (82) as a function of signal photons. The solid blue line in Fig. (8) was computed from Eq. (82) for an ideal case when there are no losses in the system ($\eta_d = \eta_h = a = o = 1$). The curve shows that for a low number of signal photons, the shot noise dominates. When the signal increases, the SNR levels off at 1. This is consistent with [11] and is a result of the laser speckle. No matter how many signal photons are received, the image SNR will not increase above 1. There are techniques to improve this limit, but those will not be discussed at a this time. For more information, see [8, 3]. The dashed blue line in Fig. (8) shows how under less ideal circumstances, $\left(\eta_d = 0.4,\ \eta_h = 0.5,\ a = 0.3,\ o = \sqrt{0.4}\right)$, the SNR shifts to the right, resulting in more signal photons being required to achieve the same SNR.

Next, we wish to compare the above results with those obtained in [8]. The green lines in Fig. (8) show Lucke's (RL) SNR for the ideal and non-ideal cases. Both SNR models have similar shapes, although the RL SNR is a bit more optimistic than the one developed in this paper. There are two reasons for this. First, the RL SNR does not account for the fact that the beams must be split for the two detectors. Second, the RL model does not include object reflectivity or transmission losses along the optical path. When those two issues are ignored, the SNR model given in Eq. (82) matches the RL model. The RL model could be easily modified to accommodate these parameters. The differences are not major, but may give unrealistic results when not considered.

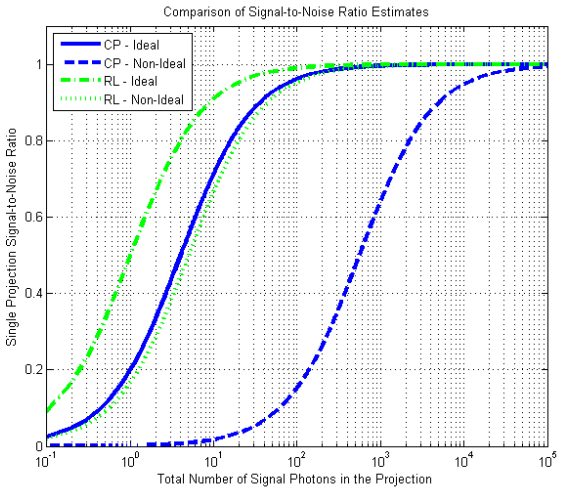

Fig. 8. SNR computed from Eq. (82), as a function of signal photons (CP, blue). SNR computed from [8] (RL, green). Both ideal and non-ideal conditions are shown.

Finally, it's helpful to apply the SNR model described in Eq. (82) to see how ISAL sample images might appear for different signal levels. Figure 9 shows eight images over a range of SNR levels. A no-noise image was formed by taking 100 radial slices through the Fourier transform of the pristine image. Then, a convolution backprojection algorithm [1] was used to reconstruct a no-noise ISAL image. Finally, Gaussian noise was added to each pixel with a mean given by the corresponding signal level $N_s o^2(z)$, and the variance was computed from Eq. (82). A Gaussian distribution was selected based on [8]. The figure highlights how ISAL images differ from conventional images. As the SNR increases, the resolution stays constant; however the ability to distinguish the object improves.

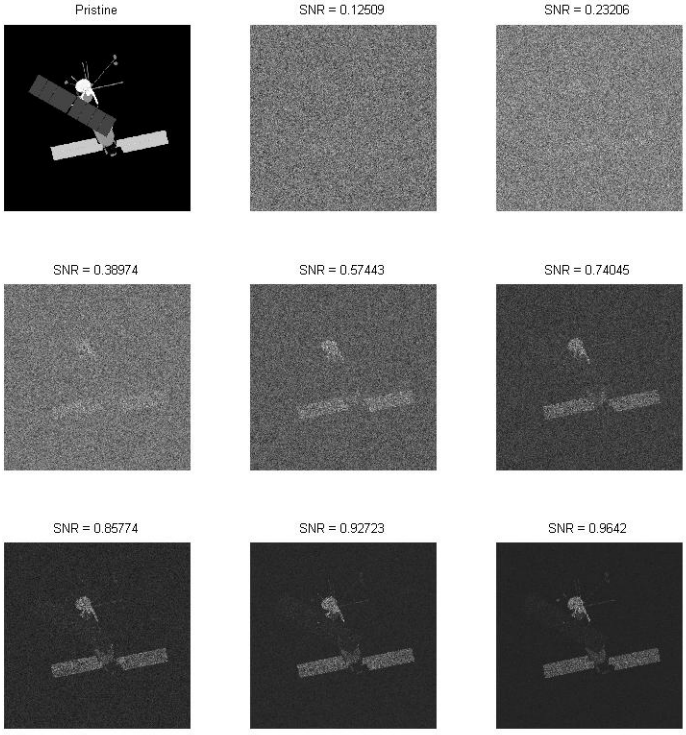

Fig. 9. Example image of C SAT for various SNR levels.

5. CONCLUSIONS

Through the above analysis, a SNR model for ISAL images has been developed using terminology and techniques common to the image processing community. Tomographic methods were used to model and explain how chirped coherent illumination results in the detection of offset Fourier data in the spatial frequency domain. Since the laser speckle acts to modulate baseband data across the Fourier domain, it allows us to reconstruct the object profile from offset data. This aspect of ISAL differentiates it from other LADAR imaging techniques. A small range of look angles can be used to image GEO space objects. While laser speckle helps us in that sense, it also limits the achievable SNR to one. In low signal levels, we saw that shot noise dominates. As the signal increases, the speckle dominates, and the SNR levels off at unity. Methods to improve ISAL SNR, will be the subject of future research. The model developed in this paper will provide a useful tool when designing an ISAL system for GEO imaging or when modeling other ISAL aspects such as transmitter power, or image improvement algorithms.

6. REFERENCES

1. A.C. Kak and M. Slaney, *Computerized Tomographic Imaging*, IEEE Press, 1998
2. D.C. Munson, J.D. O'Brien, and W.K. Jenkins, "A Tomographic Formation of Spotlight-Mode Synthetic Aperture Radar", IEEE Proceedings, Vol. 71, No. 8, 1983.
3. C.V. Jakowatz, et. al., *Spotlight-Mode Synthetic Aperture Radar: A Signal Processing Approach*, Kluwer Academic Publishers, Norwell, MA, 1996.
4. C.L. Matson, E.P. Magee, and D.E. Holland, "Reflective tomography using short-pulselength laser: system analysis for artificial satellite imaging", Op. Eng., Vol. 34 No. 9, 1995
5. R.D. Richmond and S.C. Cain, *Direct Detection LADAR Systems*, SPIE Press, 2010
6. D.C. Munson, J.L.C. Sanz, "Image Reconstruction from Frequency-Offset Fourier Data", IEEE Proceedings, Vol. 71, No. 8, 1983.
7. C.L. Matson and D.E. Mosley, "Reflective tomography reconstruction of satellite features – field results", App. Optics, Vol. 40, No. 14, 2001
8. R.L. Lucke and L.J. Rickard, "Photon-limited synthetic-aperture imaging for planet surface studies", App. Optics, Vol. 72, No. 6, 1984.
9. M.D. Desai and W.K. Jenkins, "Convolution Backprojection Image Reconstruction for Spotlight Mode Synthetic Aperture Radar", IEEE Transactions on Image Processing, Vol. 1, No. 4, 1992
10. R.M.Gagliardi and S. Karp, *Optical Communications*, John Wiley & Sons, Inc., New York, 1976
11. J. W. Goodman, *Speckle Phenomena in Optics, Theory and Applications*, Roberts & Company Publishers, Englewood, CO, 2006
12. J.W. Goodman, *Statistical Optics*, John Wiley & Sons, Inc., New York, NY, 1985
13. C.L. Matson, "Reconstructed image signal-to-noise issues in range-resolved reflective tomography", Optics Comm., 137 (1997) 343-358